White Rose Research Online
eprints@whiterose.ac.uk
https://eprints.whiterose.ac.uk
Universities of Leeds, Sheffield and York

Deposited via The University of Sheffield.

White Rose Research Online URL for this paper:
https://eprints.whiterose.ac.uk/id/eprint/238373/

Version: Accepted Version

Article:

Lone, J.A., Drummond, R., Bhaumik, S. et al. (2025) Cell-level state-estimation in parallel connected lithium-ion battery packs. European Journal of Control, 85. 101264. ISSN: 0947-3580

https://doi.org/10.1016/j.ejcon.2025.101264

© 2025 The Authors. Except as otherwise noted, this author-accepted version of a journal article published in European Journal of Control is made available via the University of Sheffield Research Publications and Copyright Policy under the terms of the Creative Commons Attribution 4.0 International License (CC-BY 4.0), which permits unrestricted use, distribution and reproduction in any medium, provided the original work is properly cited. To view a copy of this licence, visit http://creativecommons.org/licenses/by/4.0/

Reuse
This article is distributed under the terms of the Creative Commons Attribution (CC BY) licence. This licence allows you to distribute, remix, tweak, and build upon the work, even commercially, as long as you credit the authors for the original work. More information and the full terms of the licence here: https://creativecommons.org/licenses/

Takedown
If you consider content in White Rose Research Online to be in breach of UK law, please notify us by emailing eprints@whiterose.ac.uk including the URL of the record and the reason for the withdrawal request.

UNIVERSITY OF LEEDS
University of Sheffield
UNIVERSITY of York

Cell-Level State-Estimation in Parallel Connected Lithium-ion Battery Packs

Jaffar Ali Lone, Ross Drummond, Shovan Bhaumik and Nutan Kumar Tomar

***Abstract*—State estimation is essential when deploying lithium-ion (Li-ion) battery packs in the field as it enables accurate predictions of key properties, such as the remaining range of electric vehicles. Most existing studies on state estimators for battery packs have used simple, lumped models for the pack, with each cell considered equivalent. These low-resolution lumped models are not able to capture the inherent cell-to-cell variability in packs, a feature which has limited the effectiveness of state estimators. To address this issue, a Hermite polynomial-based Extended Kalman filter (HP-EKF) is proposed to estimate the states of each cell in a parallel connected battery pack described by descriptor system dynamics. The performance of the proposed cell-level state-estimator is validated in experiments with two LiNiMnCoO$_2$ Li-ion batteries connected in parallel. The model demonstrated high accuracy in predicting the response of the two parallel-connected Li-ion batteries, with root mean squared error of 0.00345V between experimental and modeled voltages. The proposed HP-EKF significantly reduces the estimation error compared to the conventional EKF while achieving accuracy comparable to the Cubature Kalman filter (CKF). Moreover, the HP-EKF exhibits computational complexity similar to the CKF while offering enhanced numerical stability by preserving the desirable properties of the error covariance matrices during implementation. This advantage, which typically requires the square-root variant of the CKF (SR-CKF), is inherently retained in the HP-EKF without the additional computational burden of the SR-CKF. These results highlight the potential of implementing cell-level estimation in parallel connected battery packs to provide information-rich estimates of its states.**

***Index Terms*—Descriptor systems, Extended Kalman filter, Parallel connected battery packs, State of charge estimation.**

NOMENCLATURE

V_{OCV}	Open circuit voltage
Z_m	State of charge of m^{th} cell
V_{Tm}	Terminal voltage of m^{th} cell
X_d	Dynamic states
X_a	Algebraic states
$\boldsymbol{H}_p$	Hermite polynomial of order p
η, ν	Process and measurement noise, respectively
$\mathcal{Q}$, $\mathcal{R}$	Process and measurement noise covariance matrices, respectively
$\hat{X}_{d,k\|k-1}$, $\hat{X}_{d,k\|k}$	Prior and posterior state estimate of dynamic states
$P_{d,k\|k-1}$, $P_{d,k\|k}$	Prior and posterior error covariance matrix of dynamic states
$P^{YY}_{d,k\|k-1}$, $P^{X_dY}_{d,k\|k}$	Prior innovation covariance matrix and Prior cross-covariance matrix.
K_k	Kalman gain
$\hat{X}_{a,k\|k}$	Posterior estimate of algebraic states
$P_{a,k\|k}$	Posterior error covariance matrix of algebraic states
S	Cholesky factor
ζ, ω	Sample points and their corresponding weights
$\mathbb{E}$	Expectation operator
$\mathfrak{C}$	Computational cost
$\mathbb{I}_n$	Identity matrix of order n
κ_d	Standard Gaussian random variable
ε_d, ε_a	Estimation error of dynamic and algebraic states, respectively
$\mathcal{N}(x; \hat{x}, P)$	Gaussian distribution with mean $\hat{x}$ and covariance P.

I. INTRODUCTION

As well as their relatively long lifespans (≈ 5,000 cycles) and low costs (101/kWh) [1], two of the main advantages of lithium-ion (Li-ion) batteries as energy storage devices are their high energy (230 to 367 Wh/L) and power densities (≈ 7 kW/L) [2]. However, even then, the power and energy demands of many of today's technologies (such as electric vehicles (EVs) and aircraft) are still beyond those of individual cells, so large battery packs have to be used instead. Battery packs are formed from interconnecting individual cells in series and parallel to form larger power units; typically with the series connections providing additional power and the parallel ones providing additional energy and more tolerance to faults [3].

Today, large battery packs are growing in numbers and in scale. Using the $nPmS$ notation to denote pack configurations, for example, large EV packs include the: Tesla Model S (74P96S), Tesla Model 3 (46P96S), VW eGolf (3P88S), Nissan Leaf (2P96S), BAIC EU260 (3P90S), Renault Zoe (2P96S) and Audi etron (4P108S) [4]. The sheer number of cells in these large packs highlights the added complexity of powering these new technologies, as well as the lack of standardisation across the field, both in terms of the design but also for the battery management system (BMS) algorithms.

However, scaling up battery packs also introduces problems. In particular, it introduces inefficiencies which can cause the energy density of the pack to be as little as 11% of the cell [2]. One of the main reasons for this loss in performance is simply

Jaffar Ali Lone thanks the Ministry of Education, Govt. of India, for providing financial support via PMRF Grant no. 2701805. Nutan K. Tomar acknowledges funding by the Science and Engineering Research Board, New Delhi, via Grant number CRG/2023/008861.

Jaffar Ali Lone and Shovan Bhaumik are with the Department of Electrical Engineering, Indian Institute of Technology Patna, India. `{jaffar_2121ee06,shovan.bhaumik}@iitp.ac.in`.

Ross Drummond is with the School of Electrical and Electronic Engineering, University of Sheffield, UK. `ross.drummond@sheffield.ac.uk`.

Nutan Kumar Tomar is with the Department of Mathematics, Indian Institute of Technology Patna, India. `nktomar@iitp.ac.in`.

that every cell in the pack behaves and degrades *uniquely* [5], [6]. Cell-to-cell variation across the pack is due to each cell having different parameters at the point of manufacture, and these parameter differences can grow in time as the cell ages [7], [8]. Experimental studies, such as [9], have revealed significant imbalances in parallel-connected cells, including a 30% variation in impedance, a 60% difference in peak cell current, and over 6% difference in charge throughput during cycling. With the performance of the pack often governed by its weakest cell, these parameter variations can have a significant impact on performance.

With every cell behaving uniquely, estimating all the states in the packs becomes a challenging problem. State estimation has revolutionised battery technology, as applications such as electric vehicles would not exist without accurate range estimates provided by an estimator. Whilst significant research has been conducted on state estimation of *individual* batteries over the years, notably [10]–[14], the analysis of *packs* has been significantly less developed. Most existing studies have avoided the problem of dealing with the complexity of the cell-level estimation problem by lumping all the cells together into one representative cell for the whole pack [10], [11]. Lumping the pack in this way greatly simplifies the problem (both analytically and computationally), but the lack of granularity in the model means cell-level information is lost. As such, there is a wealth of information unavailable to the BMS, limiting its capabilities. Another approach for pack estimation tracks only the best and worst cells in the pack [12], but this method suffers from the fact that it requires tracking these extremal cells, and they may change in time as each cell degrades at different rates. The final approach uses an array of current sensors on *each* cell to separately estimate all the states in the pack before combining these estimates to calculate the overall state-of-charge (SOC) of the pack. This method can provide the richest information to the BMS, however, as it requires sensors on every cell, it is not computationally efficient and may not be practical for large battery packs [14]. This complexity can be mitigated by considering a reduced sensing scenario with sensors placed on only a subset of the cells in the pack and algorithms being used to estimate the states of the unmeasured cells. It is this reduced sensing setup which is considered here (it is assumed that there is only a single voltage and current sensor for the pack), as the goal is to achieve a scalable cell-level estimator for the pack. See [15] for a detailed discussion and comparison of these estimation techniques.

The focus of this work is on designing state estimators for parallel connected battery packs. As has been observed in previous studies, *e.g.,* [16]–[19], parallel pack dynamics are more complex to analyse than those in series. With series connections, every cell receives the same charging current, so the state estimators for each cell can just be collected together to solve the pack-level problem. By contrast, with parallel connections, the dynamics are governed by descriptor systems, with the currents distributing themselves across the pack to satisfy Kirchhoff's laws. If the cells have different parameters (e.g. resistances and capacitances), then Kirchhoff's laws cause current imbalances and even oscillations in the response [18]. As a result of these current distributions (an example of which is shown in Section VI where there is a 21.45% difference between the branch currents of Cell 1 and 2), charge imbalances can develop across the pack, which justifies the use of a cell-level estimator.

Several methods have been developed to estimate the states of cells of parallel connected Li-ion battery packs using Luenberger observers, e.g. [16]–[18]. In [20], a unified modeling framework for battery packs was presented based on a nonlinear descriptor electrochemical model, and then a linear matrix inequality-based nonlinear state observer was proposed for the estimation purpose. An interval observer was designed for the parallel connected battery pack in [21], which improved the scalability by using upper and lower bounds for the unmeasured states. Whilst these results are all significant, they have limitations, including the lack of analysis on Kalman filter-type algorithms (even though these algorithms are popular in practice) and have not been validated experimentally. It is this research gap which is addressed by this work.

Contributions: The main contribution of this paper are:

1) A Hermite polynomial-based extended Kalman filter (HP-EKF) is proposed for cell-level state estimation of parallel connected battery packs described by descriptor systems.
2) The proposed HP-EKF significantly reduces the estimation error compared to the conventional EKF and achieves accuracy comparable to the Cubature Kalman Filter (CKF). While its computational complexity is similar to that of CKF, the HP-EKF offers improved numerical stability by preserving the desirable properties of error covariance matrices during implementation [22]. This advantage, which typically requires the square-root variant of the CKF (SR-CKF), is inherently retained in the HP-EKF without the additional computational burden of the SR-CKF.
3) The method was also validated in experiments with two $LiNiMnCoO_2$ cells connected in parallel. The model demonstrated high accuracy in predicting the response of the two parallel-connected cells, with root mean squared error (RMSE) of 0.00345V between experimental and modeled voltages.

As discussed in Section III, the HP-EKF is an orthogonal polynomial EKF which leverages the orthogonal property of the Hermite polynomial to approximate the nonlinear functions. The main advantage of using Hermite polynomials for the linearisation is that their weighting function is the same as that of the Gaussian. Hence, it allows a more accurate propagation of the noise, a fact reflected in the reduced estimation error compared to the standard EKF in both dynamic and algebraic states. Finally, by comparing the performance of the state estimator against experimental data (see Section V), these results highlight the potential of implementing cell-level estimation in the field.

II. BATTERY PACK MODEL FORMULATION

The model equations for the parallel connected Li-ion battery pack are first introduced. The equations are obtained from [16] and then implemented in an experimental setup in Section V.

A. Single Cell Model

In this paper, a second-order Thevenin equivalent circuit model (ECM) (as shown in Fig. 1) is used to describe the dynamics of each cell. With this model, the voltage source V_{OCV} describes the battery's open-circuit voltage (OCV), and R_0 is its internal resistance. The polarization resistances are R_1, R_2, the polarization capacitances are C_1, C_2, and the voltages across the R_1C_1 and R_2C_2 pairs are V_1 and V_2, respectively. The terminal voltage is denoted by V_T while I_k is the current applied to the battery.

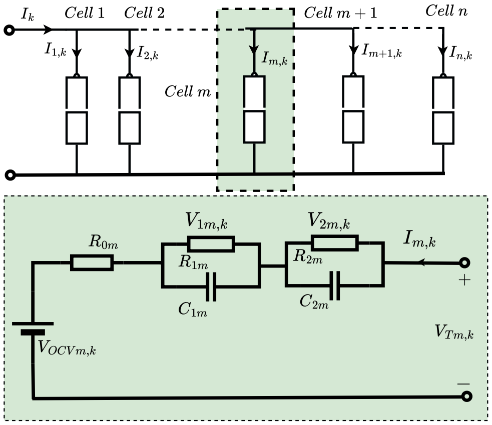

Figure 1: Second order Thevenin ECM of m^{th} cell in a parallel connected module of n cells.

Using the ECM of Fig. 1, the dynamics of the m^{th} cell in the parallel connected pack of n cells are

$$x_{m,k+1} = \tilde{A}_m x_{m,k} + \tilde{B}_m u_{m,k}, \tag{1a}$$

$$y_{m,k} = h_m(x_{m,k}) + \tilde{D}_m u_{m,k}, \tag{1b}$$

with $x_{m,k} = [Z_{m,k}\ V_{1m,k}\ V_{2m,k}]^T$ being the state vector at time step k, $Z_{m,k}$ the SOC, $V_{1m,k}$ and $V_{2m,k}$ the polarizing voltages of the RC pairs. The control input $u_{m,k} = I_{m,k}$ is the current, and $y_{m,k} = V_{Tm,k}$ is the terminal voltage of the m^{th} cell. The matrices $\tilde{A}_m$ and $\tilde{B}_m$ are parameterised by

$$\tilde{A}_m = \begin{bmatrix} 1 & 0 & 0 \\ 0 & e^{-\frac{T_s}{R_{1m}C_{1m}}} & 0 \\ 0 & 0 & e^{-\frac{T_s}{R_{2m}C_{2m}}} \end{bmatrix}, \tag{2a}$$

$$\tilde{B}_m = \begin{bmatrix} \frac{T_s}{C_{bm}} \\ R_{1m}(1 - e^{-\frac{T_s}{R_{1m}C_{1m}}}) \\ R_{2m}(1 - e^{-\frac{T_s}{R_{2m}C_{2m}}}) \end{bmatrix}, \tag{2b}$$

and $\tilde{D}_m = [R_{0m}]$. Also, $h_m(x_{m,k}) = V_{OCV_{m,k}} + V_{1m,k} + V_{2m,k}$ with $V_{OCV_{m,k}}$ being the OCV which is a nonlinear function of the SOC, $Z_{m,k}$. T_s is the sampling time.

B. Descriptor system-based Model of Parallel Connected Battery Pack

Now, consider a module of n cells connected in parallel. The dynamics of parallel connected packs are subject to Kirchhoff's laws and enforce the conservation of current and voltage across the pack. Specifically, Kirchhoff's voltage law means that all the cells in the parallel pack have the same voltage, with

$$\begin{aligned} &V_{OCV_{p,k}} + V_{1p,k} + V_{2p,k} + R_{0p}I_{p,k} \\ &\quad = V_{OCV_{q,k}} + V_{1q,k} + V_{2q,k} + R_{0q}I_{q,k} \end{aligned} \tag{3a}$$

for all $p, q \in \{1, 2, ..., n\}$. Kirchhoff's current law imposes that the total current flowing into each cell, with the notation $I_{j,k}(t)$ referring to the current flowing into cell j at time-step k, equals that applied to the pack, here referred to as I_k, as in

$$\sum_{j=1}^{n} I_{j,k} = I_k. \tag{3b}$$

Note that (3) define n algebraic constraints that the pack model must satisfy at each point in time. It is these algebraic equations which give rise to the descriptor dynamics of (5).

It is assumed that the pack is subject to a reduced sensing scenario with only the total applied current, I_k, and pack voltage, $y_k = y_{m,k}$, $m = 1, 2, \ldots, n$, known. This implies that the branch currents, $I_{1,k}\ \ I_{2,k}, \ldots, I_{n,k}$ entering each cell are not measured and have to be inferred from the estimator.

Combining the n algebraic equations of (3) from Kirchhoff's laws with the individual cell dynamics of (1) allows the pack dynamics to be expressed as a descriptor system with

$$EX_{k+1} = AX_k + \Theta(X_k), \tag{4a}$$

$$y_k = HX_k + \Phi(X_k). \tag{4b}$$

Here, $X_k = [X_{d,k},\ \ X_{a,k}]^T \in \mathbb{R}^{4n}$, $X_{d,k} \in \mathbb{R}^{3n}$ are dynamic states and $X_{a,k} \in \mathbb{R}^n$ are algebraic states with $X_{d,k} = [x_{1,k},\ x_{2,k},\ \cdots\ ,\ x_{n,k}]^T$, and $X_{a,k} = [I_{1,k},\ \ I_{2,k},\ \ \cdots\ \ ,\ \ I_{n,k}]^T$. y_k is the set of output vectors for n cells in parallel and is given by $y_k = [y_{1,k},\ y_{2,k},\ \cdots\ ,\ y_{n,k}]^T \in \mathbb{R}^n$.

As the parallel pack dynamics include both algebraic, (3), and dynamic, (1), equations the matrix E is singular. Specifically, matrices E and A are structured as

$$E = \begin{bmatrix} \mathbb{I}_{3n} & 0_{3n\times n} \\ 0_{n\times 3n} & 0_{n\times n} \end{bmatrix}, A = \begin{bmatrix} A_{11} & A_{12} \\ A_{21} & A_{22} \end{bmatrix},$$

with $\mathbb{I}_m$ being the identity matrix of dimension m and $A_{11} = diag(\tilde{A}_1,\ \tilde{A}_2,\ \cdots\ ,\tilde{A}_n)$, $A_{12} = diag(\tilde{B}_1,\ \tilde{B}_2,\ \cdots\ ,\tilde{B}_n)$,

$$A_{21} = \begin{bmatrix} \tilde{C}_1 & -\tilde{C}_1 & 0 & \cdots & 0 \\ \tilde{C}_1 & 0 & -\tilde{C}_1 & \cdots & 0 \\ \vdots & \vdots & \vdots & \ddots & \vdots \\ \tilde{C}_1 & 0 & 0 & \cdots & -\tilde{C}_1 \\ 0 & 0 & 0 & \cdots & 0 \end{bmatrix} \in \mathbb{R}^{n\times 3n},$$

$\tilde{C}_1 = [0\ 1\ 1]$,

$$A_{22} = \begin{bmatrix} R_{01} & -R_{02} & 0 & \cdots & 0 \\ R_{01} & 0 & -R_{03} & \cdots & 0 \\ \vdots & \vdots & \vdots & \ddots & \vdots \\ R_{01} & 0 & 0 & \cdots & -R_{0n} \\ 1 & 1 & 1 & \cdots & 1 \end{bmatrix} \in \mathbb{R}^{n\times n}.$$

Function $\Theta(X_k)$ contains the model's nonlinearities in (4), which emerge due to the open circuit voltage terms in Kirchhoff's laws. The vector of nonlinearities can be structured as

$$\Theta(X_k)=\left[\begin{array}{c}\Theta_d(X_k)\\ \hline \Theta_a(X_k)\end{array}\right]=\left[\begin{array}{c}0_{3n\times 1}\\ \hline V_{OCV_{1,k}}-V_{OCV_{2,k}}\\ \vdots\\ V_{OCV_{1,k}}-V_{OCV_{n,k}}\\ -I_k\end{array}\right]\in\mathbb{R}^{4n}.$$

The output (4b) models the voltage of each cell of a parallel connected battery pack with $H=[H_d\quad H_a]$, where $H_d=diag(\tilde{C}_1,\ \tilde{C}_1,\ \cdots,\ \tilde{C}_1)\in\mathbb{R}^{n\times 3n}$ and $H_a=diag(R_{01},\ R_{02},\cdots,\ R_{0n})\in\mathbb{R}^{n\times n}$, $\Phi(X_k)=[V_{OCV_{1,k}}\ \cdots\ V_{OCV_{n,k}}]^T$. Note that A_{22} is a full-rank matrix, and so the linear part of the descriptor system (4) is regular and of index-one.

Remark 1. Although this work focuses on parallel-connected battery cells, the modeling approach can be extended to series-parallel configurations by grouping cells in parallel to form modules and then connecting these modules in series. This hierarchical modeling structure reflects practical battery pack architectures used in many electric vehicles, such as Tesla Model S and Model 3 [17].

C. Model Simplification

The descriptor system (4) for the parallel pack dynamics can be divided into dynamic and algebraic states with an explicit input current, *i.e.,*

$$\begin{bmatrix}\mathbb{I}_{3n} & 0\\ 0 & 0\end{bmatrix}\begin{bmatrix}X_{d,k+1}\\ X_{a,k+1}\end{bmatrix}=\begin{bmatrix}A_{11} & A_{12}\\ A_{21} & A_{22}\end{bmatrix}\begin{bmatrix}X_{d,k}\\ X_{a,k}\end{bmatrix}+\begin{bmatrix}0\\ \Theta_I\end{bmatrix}I_k+\begin{bmatrix}\Theta_d(X_k)\\ \tilde{\Theta}_a(X_k)\end{bmatrix}, \tag{5a}$$

$$y_k=\begin{bmatrix}H_d & H_a\end{bmatrix}\begin{bmatrix}X_{d,k}\\ X_{a,k}\end{bmatrix}+\Phi(X_k), \tag{5b}$$

where $\Theta_I=\begin{bmatrix}0,\cdots,-1\end{bmatrix}^T\in\mathbb{R}^n$, and $\tilde{\Theta}_a(X_k)=\Theta_a(X_k)-\Theta_I I_k$. Simplifying (5a), we obtain

$$X_{d,k+1}=A_{11}X_{d,k}+A_{12}X_{a,k}+\Theta_d(X_k), \tag{6a}$$

$$0=A_{21}X_{d,k}+A_{22}X_{a,k}+\Theta_I I_k+\tilde{\Theta}_a(X_k). \tag{6b}$$

Since A_{22} is invertible, then from (6b), we have

$$X_{a,k}=-{A_{22}}^{-1}[A_{21}X_{d,k}+\Theta_I I_k+\tilde{\Theta}_a(X_k)]. \tag{7}$$

Substituting (7) into (6a) and simplifying gives

$$X_{d,k+1}=f(X_{d,k})+BI_k+\eta_k, \tag{8a}$$

$$X_{a,k}=-{A_{22}}^{-1}(A_{21}X_{d,k}+\Theta_I I_k+\tilde{\Theta}_a(X_{d,k})), \tag{8b}$$

$$Y_k=g(X_{d,k})+\nu_k, \tag{8c}$$

where

$$\begin{aligned}f(X_{d,k})\ &=(A_{11}-A_{12}{A_{22}}^{-1}A_{21})X_{d,k}\\ &\quad-A_{12}{A_{22}}^{-1}\tilde{\Theta}_a(X_{d,k})+\Theta_d(X_k),\\ g(X_{d,k})\ &=(H_d-H_a{A_{22}}^{-1}A_{21})X_{d,k}\\ &\quad-H_a{A_{22}}^{-1}\tilde{\Theta}_a(X_{d,k})+\Phi(X_{d,k}),\end{aligned}$$

$B=A_{12}{A_{22}}^{-1}\Theta_I$, and $Y_k=y_k-H_a{A_{22}}^{-1}\Theta_I I_k$. Moreover, process noise η_k and measurement noise ν_k have been added to the system dynamics as it was observed in experimental data (see Section V). From the data, it was assumed that η_k and ν_k are white, Gaussian and uncorrelated to each other with zero mean, covariance $\mathcal{Q}_k$ and $\mathcal{R}_k$, respectively, *i.e.,* $\mathbb{E}[\eta_k\nu_j^T]=0$, $\mathbb{E}[\eta_k\eta_j^T]=\mathcal{Q}_k\delta_{kj}$ and, $\mathbb{E}[\nu_k\nu_j^T]=\mathcal{R}_k\delta_{kj}$, where δ_{kj} is the Kronecker delta, $\mathcal{Q}_k$ and $\mathcal{R}_k$ are symmetric positive definite matrices.

III. Hermite Polynomial Based Extended Kalman Filtering Algorithm (HP-EKF)

This section gives the mathematical description of the HP-EKF proposed in this paper for cell-level state estimation of parallel connected Li-ion battery packs. In orthogonal polynomial-based EKF methods, orthogonal polynomial expansions are used to linearise the nonlinear systems [23], [24]. The HP-EKF proposed in this work is a specific instance of such filters which utilizes Hermite polynomial expansion for linearization. This filtering technique is different from the conventional EKF in the sense that the linearization process is not done using Taylor series approximation; rather, it is done using first-order Hermite polynomials. Important to mention here that the Taylor series approximation is a purely local approximation and not optimal in any norm. Its accuracy degrades rapidly away from the nominal point. Therefore, the HP-EKF is anticipated to perform better than the Taylor series-based EKF since the chosen basis is optimal with respect to the Gaussian measure [25], [26], and linearization is used principally to integrate with respect to the Gaussian measure. Moreover, the HP-EKF is designed to be more robust, effectively maintaining the desirable properties of error covariance matrices during implementation. In Kalman filtering, square root versions of filters, like the Square Root Cubature Kalman Filter (SR-CKF) *etc.*, are often used to enhance numerical stability and ensure that covariance matrices remain positive-definite, addressing potential issues, such as the Cholesky decomposition errors when a matrix is nearly singular or poorly conditioned [22], [27]. However, the HP-EKF offers a key advantage by avoiding this issue while still ensuring accurate and reliable performance. In addition, the HP-EKF provides almost similar accuracy to its square root counterparts but with significantly lower computational costs; please see Section IV-D for details.

A. Approximatation using Hermite polynomials

Any arbitrary nonlinear function $f(x):\mathbb{R}^n\rightarrow\mathbb{R}^m$, where x is a Gaussian random variable, can be approximated with first-order Hermite polynomials [23], [28], as follows

$$f(x)\approx\boldsymbol{A_0}\boldsymbol{H_0}(x)+\boldsymbol{A_1}\boldsymbol{H_1}(x), \tag{9}$$

where $\boldsymbol{H_0}(x)$ and $\boldsymbol{H_1}(x)$ are the zero and first order Hermite polynomials while $\boldsymbol{A_0}\in\mathbb{R}^{n\times 1}$ and $\boldsymbol{A_1}\in\mathbb{R}^{n\times m}$ are the coefficient matrices calculated by

$$\boldsymbol{A_i}=\langle f(x),\boldsymbol{H_i}(x)\rangle=\int_{-\infty}^{\infty}f(x)\boldsymbol{H_i}(x)^T\mathcal{N}(x;\hat{x},\,P)dx. \tag{10}$$

In the above, $\langle , \rangle$ is the inner product, $\mathcal{N}(x; \hat{x}, P)$, represents the Gaussian distribution with mean $\hat{x}$ and covariance P. Only the first two terms of the Hermite polynomial expansion are used for the linear approximation of the state estimator's model dynamics, with the higher-order terms neglected. The main reason for choosing Hermite polynomials for the linearisation is that its weighting function is the same as that of the Gaussian (which brings advantages for Kalman filtering, due to its Gaussian assumptions on the noise). This alignment ensures that the integral approximations employed in the filtering process are optimally weighted, thereby enhancing the accuracy of state estimation. Furthermore, in the Taylor series approximation, the error may be small near the nominal point, but it increases rapidly with the distance from the nominal point [24]. However, the functional approximation based on the orthogonal polynomials, such as Hermite polynomials, provides a good approximation in an entire region (the $\mathcal{L}_2$ space), as the best approximation in the 2-norm is closely related to the notion of orthogonality [25, see p. 252] and Hermite polynomials satisfy the property of orthogonality [28], *i.e.,*

$$\langle \boldsymbol{H_i}(x), \boldsymbol{H_j}(x) \rangle = \begin{cases} \mathbb{I}_n & \text{if } i = j, \\ 0 & \text{otherwise.} \end{cases} \tag{11}$$

B. Linearisation with Hermite polynomials

Taking a Cholesky decomposition of the matrix $P = SS^T$, with S being the square root matrix of P, then it is easy to verify that $\boldsymbol{H_0}(x) = 1$ and $\boldsymbol{H_1}(x) = S^{-1}(x - \hat{x})$. Substituting $\boldsymbol{H_0}(x)$ and $\boldsymbol{H_1}(x)$ into (9) implies

$$f(x) \approx \boldsymbol{A_0} + \boldsymbol{A_1} S^{-1}(x - \hat{x}). \tag{12}$$

It is important to highlight that this method of linearisation is fundamentally different from the gradient-based linearisation of the standard EKF. The Taylor series approximation is a purely local approximation and not optimal in any norm, and so its accuracy can degrade rapidly away from the nominal point. Hence, the proposed filter based on Hermite polynomial linearisation is anticipated to perform better than the Taylor series-based EKF since the chosen basis is optimal with respect to the Gaussian measure [25], [26], and linearisation is used principally to integrate with respect to the Gaussian measure. Foreshadowing the results of this paper, Section V validates this hypothesis, as the estimation error is reduced significantly. Following (12), the nonlinearities in the dynamic, algebraic, and measurement equations in (8) are linearised by

$$f(X_{d,k}) = F_{2,k} + F_{1,k} S_{k|k-1}^{-1}(X_{d,k} - \hat{X}_{d,k}), \tag{13a}$$

$$g(X_{d,k}) = G_{2,k} + G_{1,k} S_{k|k-1}^{-1}(X_{d,k} - \hat{X}_{d,k}), \tag{13b}$$

$$\tilde{\Theta}_a(X_{d,k}) = \theta_{2,k} + \theta_{1,k} S_{k|k-1}^{-1}(X_{d,k} - \hat{X}_{d,k}), \tag{13c}$$

where $F_{1,k},\ F_{2,k},\ G_{1,k},\ G_{2,k},\ \theta_{1,k}$, and $\theta_{2,k}$ are the matrices constructed using (10) by

$$F_{1,k} = \int_{-\infty}^{\infty} f(X_{d,k})(S_{k|k-1}^{-1}(X_{d,k} - \hat{X}_{d,k}))^T \\ \mathcal{N}(X_{d,k}; \hat{X}_{d,k|k-1}, P_{k|k-1}) dX_{d,k}, \tag{14a}$$

$$F_{2,k} = \int_{-\infty}^{\infty} f(X_{d,k}) \mathcal{N}(X_{d,k}; \hat{X}_{d,k|k-1}, P_{k|k-1}) dX_{d,k}, \tag{14b}$$

$$G_{1,k} = \int_{-\infty}^{\infty} g(X_{d,k})(S_{k|k-1}^{-1}(X_{d,k} - \hat{X}_{d,k}))^T \\ \mathcal{N}(X_{d,k}; \hat{X}_{d,k|k-1}, P_{k|k-1}) dX_{d,k}, \tag{14c}$$

$$G_{2,k} = \int_{-\infty}^{\infty} g(X_{d,k}) \mathcal{N}(X_{d,k}; \hat{X}_{d,k|k-1}, P_{k|k-1}) dX_{d,k}, \tag{14d}$$

$$\theta_{1,k} = \int_{-\infty}^{\infty} \tilde{\Theta}_a(X_{d,k})(S_{k|k-1}^{-1}(X_{d,k} - \hat{X}_{d,k}))^T \\ \mathcal{N}(X_{d,k}; \hat{X}_{d,k|k-1}, P_{k|k-1}) dX_{d,k}, \tag{14e}$$

$$\theta_{2,k} = \int_{-\infty}^{\infty} \tilde{\Theta}_a(X_{d,k}) \mathcal{N}(X_{d,k}; \hat{X}_{d,k|k-1}, P_{k|k-1}) dX_{d,k}. \tag{14f}$$

The integrals of (14) can not be solved analytically for any arbitrary nonlinear function [29], and so approximations have to be used instead. Various methods have been proposed to approximate these integrals, including those based on the: unscented transformation, spherical radial cubature rule, cubature quadrature, Gauss-Hermite quadrature rule, and high-degree cubature quadrature rule [30]. In this work, the third-degree spherical radial cubature rule is used to evaluate the integrals (14) to reduce the computational cost whilst maintaining comparable estimation accuracy for the experimental implementation as described in Section V.

C. Evaluation of Integrals Using Cubature Rule

In this method, the integrals of (14) are decomposed into surface and line integrals. To solve the surface integral, a third-degree spherical radial cubature rule is used here. Similarly, a first-order Gauss-Laguerre quadrature rule is used here to evaluate the line integral. For a detailed derivation of this method, see [30].

In order to calculate the coefficient matrices $F_{1,k},\ F_{2,k},\ G_{1,k},\ G_{2,k},\ \theta_{1,k}$, and $\theta_{2,k}$ using the cubature rule, the integrals in (14) need to be transformed into standard Gaussian integrals. Transforming $X_{d,k}$ into the standard Gaussian random variable, $\kappa_{d,k}$ such that $X_{d,k} = \hat{X}_{d,k|k-1} + S_{k|k-1}\kappa_{d,k}$ with the points, ζ_i, and weights, ω_i, then, defining $\chi_{i,k|k-1} = \hat{X}_{d,k|k-1} + S_{k|k-1}\zeta_i$, the integrals in (14a) and (14b) can be expressed in the required form as

$$\begin{aligned} F_{1,k} &= \sum_{i=1}^{m} f(\hat{X}_{d,k|k-1} + S_{k|k-1}\zeta_i)\zeta_i^T \omega_i \\ &= \sum_{i=1}^{m} f(\chi_{i,k|k-1})\zeta_i^T \omega_i, \end{aligned} \tag{15a}$$

$$F_{2,k} = \sum_{i=1}^{m} f(\hat{X}_{d,k|k-1} + S_{k|k-1}\zeta_i)\omega_i = \sum_{i=1}^{m} f(\chi_{i,k|k-1})\omega_i. \tag{15b}$$

Similarly, we calculate the other coefficient matrices as follows, $G_{1,k} = \sum_{i=1}^{m} g(\chi_{i,k|k-1})\zeta_i^T \omega_i$, $G_{2,k} = \sum_{i=1}^{m} g(\chi_{i,k|k-1})\omega_i$, $\theta_{1,k} = \sum_{i=1}^{m} \tilde{\Theta}_a(\chi_{i,k|k-1})\zeta_i^T \omega_i$, and $\theta_{2,k} = \sum_{i=1}^{m} \tilde{\Theta}_a(\chi_{i,k|k-1})\omega_i$.

IV. HP-EKF Algorithm Derivation

The EKF algorithm derived using Hermite polynomials which is used for cell-level state-estimation in Section V can then be obtained using the coefficient matrices $F_{1,k}$, $F_{2,k}$, $G_{1,k}$, $G_{2,k}$, $\theta_{1,k}$, and $\theta_{2,k}$ calculated in (15). Using (13) and substituting $f(X_{d,k})$, $g(X_{d,k})$ and $\tilde{\Theta}_a(X_{d,k})$ into (8) gives the linearised descriptor system

$$X_{d,k+1} = F_{1,k}\kappa_{d,k} + BI_k + F_{2,k} + \eta_k, \tag{16a}$$

$$X_{a,k} = -{A_{22}}^{-1}(A_{21}X_{d,k} + \Theta_I I_k + \theta_{1,k}\kappa_{d,k} + \theta_{2,k}), \tag{16b}$$

$$Y_k = G_{1,k}\kappa_{d,k} + G_{2,k} + \nu_k. \tag{16c}$$

It emphasised that $\kappa_{d,k}$ follows a standard normal distribution. Given the linearised system (16) in the prediction step, the posterior estimate and error covariance of dynamic states are then propagated forward in time as the algebraic states can be computed from dynamic states as long as the algebraic constraints are satisfied [31]. At the end of the prediction step, the error covariance of the algebraic states and the cross-covariance matrices of errors in algebraic and dynamic states are obtained using the linearised algebraic equation. Similarly, in the update step, only the error covariance matrix of the dynamic states is directly updated from the measurements. The error covariance matrix of the updated algebraic states is not needed in the subsequent prediction step and hence is not computed directly [32].

A. Prediction Step

The prior estimate of the dynamic state vector is

$$\begin{aligned}\hat{X}_{d,k|k-1} &= \mathbb{E}[X_{d,k}|Y_{1:k-1}],\\ &= \int_{-\infty}^{\infty}(F_{1,k-1}\kappa_{d,k-1} + BI_{k-1} + F_{2,k-1} + \eta_{k-1})\\ &\quad \times \mathcal{N}(\kappa_{d,k-1};0,\mathbb{I})d\kappa_{d,k-1},\end{aligned}$$

or

$$\hat{X}_{d,k|k-1} = BI_{k-1} + F_{2,k-1}. \tag{17}$$

Let $\varepsilon_{d,k|k-1} = X_{d,k} - \hat{X}_{d,k|k-1}$ be the prior error of the dynamic states. The error covariance is then calculated by

$$\begin{aligned}P_{d,k|k-1} &= \mathbb{E}[\varepsilon_{d,k|k-1}\varepsilon^T_{d,k|k-1}]\\ &= \int_{-\infty}^{\infty}(F_{1,k-1}\kappa_{d,k-1}\kappa^T_{d,k-1}F^T_{1,k-1})\\ &\quad \mathcal{N}(\kappa_{d,k-1};0,\mathbb{I})d\kappa_{d,k-1} + \mathcal{Q}_{k-1},\end{aligned}$$

or

$$P_{d,k|k-1} = F_{1,k-1}F^T_{1,k-1} + \mathcal{Q}_{k-1}. \tag{18}$$

B. Update Step

The estimated value of the measurement and its covariance are computed from

$$\begin{aligned}\hat{Y}_{k|k-1} &= \mathbb{E}[Y_k|Y_{1:k-1}]\\ &= \int_{-\infty}^{\infty}(G_{1,k}\kappa_{d,k} + G_{2,k} + \nu_k)\mathcal{N}(\kappa_{d,k};0,\mathbb{I})d\kappa_{d,k},\\ &= G_{2,k},\end{aligned} \tag{19}$$

and

$$\begin{aligned}P^{YY}_{d,k|k-1} &= \mathbb{E}[(Y_k - \hat{Y}_{k|k-1})(Y_k - \hat{Y}_{k|k-1})^T],\\ &= \int_{-\infty}^{\infty}(G_{1,k}\kappa_{d,k}\kappa^T_{d,k}G^T_{1,k})\mathcal{N}(\kappa_{d,k};0,\mathbb{I})d\kappa_{d,k} + \mathcal{R}_k,\\ &= G_{1,k}G^T_{1,k} + \mathcal{R}_k.\end{aligned} \tag{20}$$

The cross-covariance between the dynamic states and the measurement can be calculated as

$$\begin{aligned}P^{X_dY}_{d,k|k-1} &= \mathbb{E}[(X_{d,k} - \hat{X}_{d,k|k-1})(Y_k - \hat{Y}_{k|k-1})^T],\\ &= \int_{-\infty}^{\infty}S_{k|k-1}\kappa_{d,k}\kappa^T_{d,k}G^T_{1,k}\mathcal{N}(\kappa_{d,k};0,\mathbb{I})d\kappa_{d,k},\\ &= S_{k|k-1}G^T_{1,k}.\end{aligned} \tag{21}$$

The posterior mean and covariance for the dynamic states are calculated by

$$\hat{X}_{d,k|k} = \hat{X}_{d,k|k-1} + K_k(Y_k - \hat{Y}_{k|k-1}), \tag{22a}$$

$$P_{d,k|k} = P_{d,k|k-1} - K_k P^{YY}_{d,k|k-1}K^T_k, \tag{22b}$$

with the Kalman gain, K_k, obtained from

$$K_k = P^{X_dY}_{d,k|k-1}(P^{YY}_{d,k|k-1})^{-1}. \tag{23}$$

As long as algebraic constraints are satisfied [31], then the algebraic states can be expressed in terms of the dynamic states. Therefore, from (16b), the expression for the posterior mean of the algebraic states can be written directly as

$$\hat{X}_{a,k|k} = -{A_{22}}^{-1}(A_{21}\hat{X}_{d,k|k} + \Theta_I I_k + \theta_{1,k}\hat{\kappa}_{d,k|k} + \theta_{2,k}). \tag{24}$$

The estimation error of algebraic states is given by

$$\varepsilon_{a,k|k} = X_{a,k} - \hat{X}_{a,k|k} = -{A_{22}}^{-1}A_{21}\varepsilon_{d,k|k} - {A_{22}}^{-1}\theta_{1,k}\varepsilon_\kappa, \tag{25}$$

where $\varepsilon_\kappa = \kappa_{d,k} - \hat{\kappa}_{d,k|k}$. Finally, using $P_\kappa = \mathbb{E}[\varepsilon_\kappa\varepsilon_\kappa^T]$, the posterior error covariance of the algebraic states is computed

$$\begin{aligned}P_{a,k|k} =& \mathbb{E}[\varepsilon_{a,k|k}\varepsilon^T_{a,k|k}],\\ =& A_{22}^{-1}A_{21}P_{d,k|k}(A_{22}^{-1}A_{21})^T + A_{22}^{-1}\theta_{1,k}P_\kappa(A_{22}^{-1}\theta_{1,k})^T.\end{aligned} \tag{26}$$

The whole HP-EKF procedure is summarized in Algorithm 1.

Algorithm 1 Proposed HP-EKF Algorithm

```
Step 1: Initialization
  • Initialize the filter with $\hat{X}_{d,0|0}$, and $P_{d,0|0}$.
  • Compute the sample points $\zeta_i$ and the corresponding weights $\omega_i$.
Step 2: Time Update
  • Compute $\hat{X}_{d,k|k-1}$ and $P_{d,k|k-1}$ from (17) and (18).
Step 3: Measurement Update
  • Calculate $Y_{k|k-1}$, $P^{YY}_{d,k|k-1}$, and $P^{X_dY}_{d,k|k-1}$ from equations (19)-(21).
  • Compute the $K_k$ from (23).
  • Compute the $\hat{X}_{d,k|k}$ and $P_{d,k|k}$ from (22a) and (22b).
Step 4: Estimation of Algebraic States
  • Compute $\hat{X}_{a,k|k}$ and $P_{a,k|k}$ using (24) and (26).
```

C. Eliminating the Need for Square-Root Implementation

As discussed earlier, in deterministic sample point filters, Cholesky decomposition is required to be performed at each step during which round-off error occurs due to the limited arithmetic precision of the softwares like MATLAB/Simulink [22], [27]. The numerical error accumulated over time leads the covariance matrix to lose positive definiteness, and Cholesky decomposition cannot be performed which forces the filter to stop. The proposed HP-EKF is free from this problem, and the covariance matrices preserve the property of symmetry and positive definiteness during software simulation.

From the expression of prior error covariance (18), it can be seen that the covariance matrix, $P_{d,k|k-1}$ preserves the property of symmetry and positive definiteness, and Cholesky decomposition can be calculated at each iteration of the measurement update step. The expression of posterior error covariance is

$$\begin{aligned} P_{d,k|k} &= P_{d,k|k-1} - K_k P^{YY}_{d,k|k-1} K_k^T, \\ &= P_{d,k|k-1} - (K_k S^{YY}_{k|k-1})(K_k S^{YY}_{k|k-1})^T, \end{aligned}$$

which further can be written as [33, see p. 206]

$$\begin{aligned} P_{d,k|k} = (\mathbb{I} - K_k G_{1,k} S^{-}_{k|k-1}) P_{d,k|k-1} (\mathbb{I} - K_k G_{1,k} S^{-}_{k|k-1})^T \\ + K_k \mathcal{R}_k K_k^T. \end{aligned}$$

As mentioned in [33, see p. 206], this expression for the posterior error covariance is less sensitive to roundoff error and preserves symmetry as well as positive definiteness. This is a property inherited from the EKF, even though we are using a different form of linearization.

D. Computational Complexity

Computational complexity, often measured in terms of floating-point operations (flops), provides an estimation of the computational resources required to execute an algorithm or a specific process [34]. A flop is defined as one basic algebraic operation, such as addition, subtraction, multiplication, and division, between any two floating point numbers [23]. Our proposed filtering algorithm consists of several matrix operations, including addition, multiplication, inverse, Cholesky decomposition *etc*. The addition of two matrices with dimension $p \times q$ requires pq flops. For multiplication of $p \times q$ and $q \times r$ matrix, $pr(2q-1)$ flops are required. The inverse and Cholesky decomposition of any $n \times n$ matrix demands n^3 and $n^3/3 + 2n^2$ flops, respectively [35].

Let n_d, n_a, and p be the dimension of dynamic states, algebraic states, and measurement, respectively. Then, with m sample points, the flops count of the HP-EKF is given by

$$\begin{aligned} \mathfrak{C}_{HP-EKF} = (6n_d^2 + (3+2p)n_d + 3p)m + \frac{8}{3}n_d^3 + 3n_d^2 - n_a^2 \\ + 6p^2 n_d + (2 + 2n_d + 2n_a - 1)n_d n_a - n_a \\ + 2p(2n_d - 1)n_d + p^3 + p. \end{aligned} \tag{27}$$

In order to facilitate a comprehensive comparison, we further evaluate the computational complexity of the EKF, CKF, and SR-CKF, which are given as [23], [35]

$$\begin{aligned} \mathfrak{C}_{EKF} = 8n_d^3 + (3 + 2n_d)n_d n_a + (6p + 10n_d)pn_d \\ + n_d^2 - n_d - n_a^2 - n_a + p^3. \end{aligned} \tag{28}$$

$$\begin{aligned} \mathfrak{C}_{CKF} = (6n_d^2 + (4+2p)n_d + 3p + 2p^2)m + \frac{2}{3}n_d^3 - n_a^2 \\ + (7 + 2p + 2n_a)n_d^2 + (2 + 2n_a - 1)n_d n_a - n_a \\ + (3 + 4n_d)p^2 + p(2n_d + 1) + p^3. \end{aligned} \tag{29}$$

$$\begin{aligned} \mathfrak{C}_{SR-CKF} = (8n_d^2 + (6+4p)n_d + 4p + 2p^2)m + 2n_d^3 - n_a^2 \\ + (2p + 2n_a)n_d^2 + (2 + 2n_a - 1)n_d n_a - n_a \\ + 4n_d p^2 + p + 2p^3. \end{aligned} \tag{30}$$

The flops count of these filters as a function of the number of parallel-connected cells is plotted in Fig. 2. As evident from Fig. 2, for a smaller number of cells, the flops count of the filters appears to coincide. However, the flops count of the SR-CKF is (always) higher than the proposed HP-EKF. For a specific case of two parallel-connected cells, Table I summarizes the flops count and relative execution time of the filters. As evident from Table I, the proposed HP-EKF has a computational cost comparable to that of CKF while being significantly lower than that of SR-CKF. Despite this reduced computational burden, the HP-EKF retains the advantages of the SR-CKF, making it an efficient alternative. Compared to the CKF, the HP-EKF exhibits similar computational complexity and estimation performance. However, its key advantage lies in improved numerical stability, which, in the CKF framework, is typically achieved through its square-root variant (SR-CKF) [22]. Numerical stability is a key property for the BMS state-estimators deployed in the field, as these algorithms need to provide a reliable, robust, and resilient service. By providing this numerical stability without sacrificing on computational time, the HP-EKF is a good trade-off between the CKF and the SR-CKF. This well-rounded performance indicates the potential of HP-EKFs for pack-level state-estimation. This claim is supported by the experimental results of Section V and shows the practicality of HP-EKFs for pack BMS algorithms.

Table I: Flops count and execution time comparison

Filters	Flops Count	Relative Exec. Time
EKF	2804	1.00
HP-EKF	4396	2.92
CKF	4218	2.63
SR-CKF	5546	4.24

V. EXPERIMENTAL VALIDATION AND DISCUSSION

This section details the implementation of the HP-EKF to implement cell-level state estimation on a parallel connected Li-ion battery pack under a reduced sensing scenario.

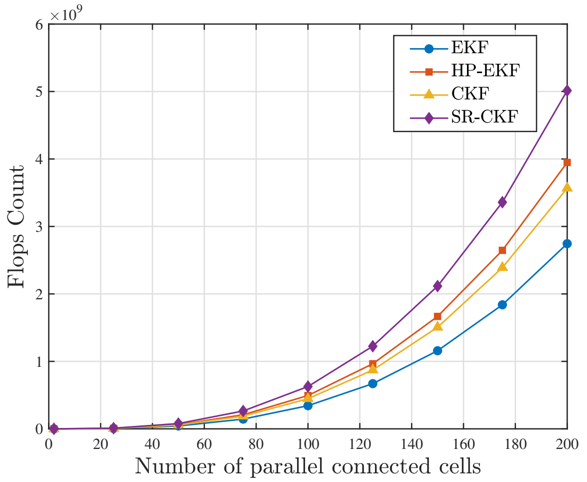

Figure 2: Plot of flops count versus the number of cells in parallel of the EKF, HP-EKF, CKF and SR-CKF

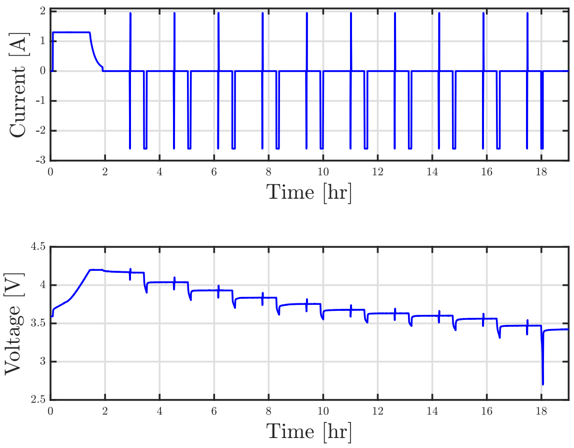

Figure 3: Current and terminal voltage profile during HPPC test.

A. Experimental Setup

A schematic of the considered parallel-connected cell pair is shown in Fig. 6. The battery test bench consists of two fresh cylindrical nickel manganese cobalt (NMC) based lithium-ion cells with capacities of 2.6 Ah connected in parallel. The detailed specifications of this NMC cell are listed in Table II. The experimental setup is shown in Fig. 7. $ACS712$ Hall effect sensors with a $20A$ range were used to measure the currents flowing into each cell. The data acquisition system consisted of an Arduino Uno microcontroller, a real-time clock, $DS3231RTC$, and an SD card module. The $DS3231RTC$ provided accurate timekeeping for data logging while the SD card module stored data for further analysis. A DC load was employed to simulate various current conditions experienced by the Li-ion cells. We used *ITECH DC Electronic Load (IT8513+)* with specifications, 120V/120A/600W.

Table II: Specifications of the NMC Cell

Parameter	**Value**
Rated Capacity	*2.6 Ah*
Nominal Voltage	*3.7 V*
Discharging End Voltage	*2.75 V*
Charging End Voltage	*4.2 V*
Charge Cut-off Current	*26 mA*
Max. Continuous Discharge Current	*7.8 A*

B. Battery Model Parameter Identification

Identifying battery model parameters is crucial for accurately predicting the performance, efficiency, and lifespan of a battery. By accurately identifying these parameters, we can improve the battery's reliability and optimize its usage in various applications. In order to identify the battery parameters, a hybrid pulse power characteristic (HPPC) test [36] on both the cells was conducted, as shown in Fig. 3. The test starts by first charging the cells fully with the constant current constant voltage (CC-CV) technique. Then the following steps are followed in the sequential order in the HPPC test: i) a 10 second discharge pulse at 1C, ii) a 40 second rest period, iii) a 10 second charging pulse at 0.75C, iv) a rest period for 30 minutes, v) a 6 minute discharge cycle at 1C (resulting in a 10% drop in SOC), vi) a rest period of 1 hour, and vii) repeat steps $(1)-(6)$, ten times.

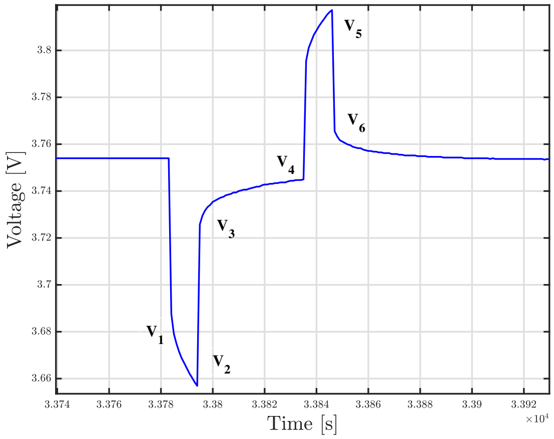

Figure 4: Transient response of terminal voltage towards charge/discharge pulses

To capture the battery's dynamic and steady-state performance accurately, a 40-second rest time is adequate after a 10-second discharge/charge pulse, while a 1-hour rest time is sufficient after a 6-minute discharge period. These rest periods allow the battery to reach a charge equilibrium state before proceeding with the next cycle [36].

1) Parameters of cell dynamics

The parameters of the second-order ECM $(R_0, R_1, R_2, C_1$ and $C_2)$ were obtained by applying the exponential-function fitting technique on the transient response of the terminal voltage during the HPPC test [36]. Fig. 4 illustrates the voltage's transient response during the pulsed discharge and charge period of each test cycle, which can be modelled as

$$V_T = V_{OCV} + R_0 I + R_1 I e^{-t/\tau_1} + R_2 I e^{-t/\tau_2}, \qquad (31)$$

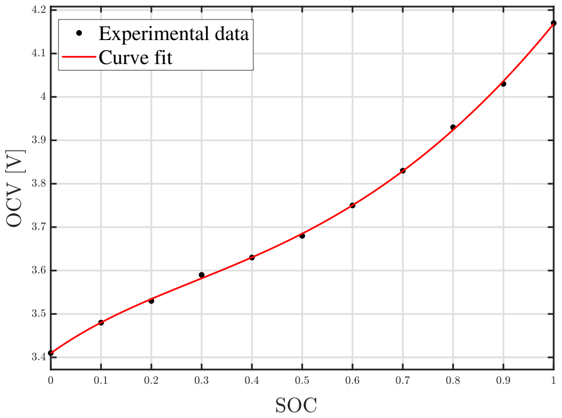

Figure 5: Experimental and curve fit for SOC-OCV relationship.

with $\tau_1 = R_1 C_1$, and $\tau_2 = R_2 C_2$. The ohmic resistance is responsible for the step change in terminal voltage at the instant the current switches [36]. Therefore, from Fig. 4, the value of R_0 when discharging is calculated from $R_0 = |\frac{V_2 - V_3}{I}|$ and when charging mode it is $R_0 = |\frac{V_5 - V_6}{I}|$. The identified parameters for cell 1 and cell 2 are shown in Table III.

Table III: Parameters of the ECM for both Cell 1 and 2.

SOC	$R_0 [m\Omega]$	$R_1 [m\Omega]$	$R_2 [m\Omega]$	C_1[F]	C_2[F]
Cell 1					
1	30.7	78.1	0.458	6287	4863
0.9	26.2	84.1	0.190	7758	5234
0.8	25.8	87.7	0.405	9300	2618
0.7	26.0	57.8	0.650	8912	1089
0.6	25.5	41.8	0.103	12800	7996
0.5	26.1	33.2	0.846	15622	4247
0.4	26.5	40.5	0.225	4567	6051
0.3	26.9	52.9	0.687	12977	1686
0.2	28.2	13.3	0.868	7262	1338
0.1	30.9	16.4	0.269	6723	3898
Cell 2					
1	27.8	58.9	0.380	5683	4319
0.9	26.3	81.6	0.861	8018	1566
0.8	25.7	84.6	0.451	9069	2052
0.7	25.8	10.0	0.625	10183	2513
0.6	25.6	40.8	0.210	12284	5445
0.5	26.1	13.8	0.133	11579	1203
0.4	26.5	36.7	0.199	17433	5905
0.3	27.3	49.5	0.321	11832	3939
0.2	28.3	21.3	0.162	4744	9443
0.1	30.0	67.3	0.154	7749	2410

2) *Open circuit voltage*

Accurate approximation of the open circuit voltage curve is crucial for accurate SOC estimation algorithms. Using the experimental data, a fifth-order polynomial approximation for the OCV curve was obtained

$$\begin{aligned} V_{OCV}(Z_{m,k}) = {} & 3.41 + 0.8287\, Z_{m,k} - 1.432\, {Z_{m,k}}^2 \\ & + 2.301\, {Z_{m,k}}^3 - 1.253\, {Z_{m,k}}^4 + 0.3136\, {Z_{m,k}}^5. \end{aligned} \tag{32}$$

A satisfactory fit was obtained, as shown in Fig. 5, which compares this polynomial approximation for the OCV curve against experimental data. To support this claim, we calculated the RMSE between the experimental data and the polynomial approximation, which was found to be 0.00416V. This low RMSE demonstrates that the fifth-order polynomial provides a highly accurate and reliable representation of the SOC-OCV relationship. It is important to mention here that we investigate the scenario where the cells are subject to the same SOC-OCV relationship but may have different initial SOCs and model parameters. This is based on the fact that the OCV-SOC relationship is a thermodynamic property and merely a function of the electrode material. In contrast to other parameters like capacity, resistance, *etc.*, the SOC-OCV change is hence likely to be unaffected by processing variation at the material level [17].

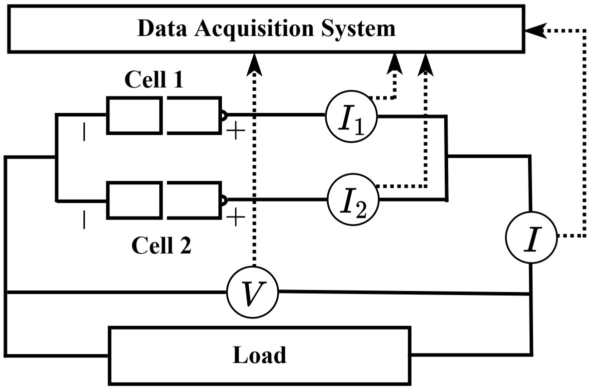

Figure 6: Schematic of the battery test bench.

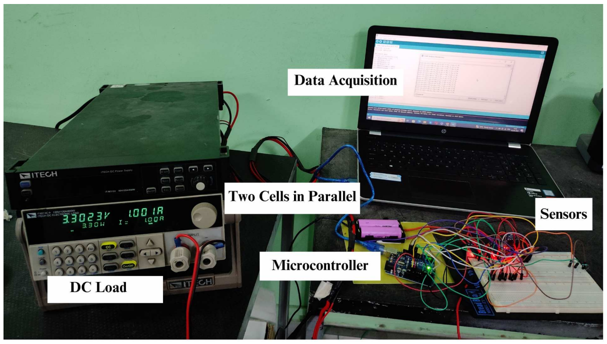

Figure 7: Hardware setup of the battery test bench.

VI. RESULTS AND DISCUSSION

A. *Model Validation*

Fig. 8 compares the experimental data with the model simulations. The RMSE between the experimental and modeled voltages, as shown in Fig. 8(a), was 0.00345 V, indicating that the model accurately predicts the response of these two parallel-connected Li-ion cells. Similarly, the experimental versus modeled comparison for the branch currents is shown in Fig. 8(b)-(c), where the RMSE for Cell 1 was 0.0902 A and for Cell 2, it was 0.0663 A, highlighting the potential to accurately model both the entire pack and the individual cells.

Unlike conventional validation approaches that use data from the HPPC test itself, our approach focused on validating the model in the context of parallel-connected cells. Due to the absence of controlled testing equipment, such as a cell

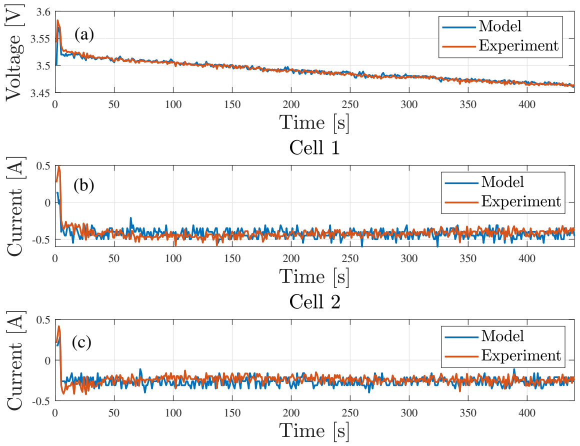

Figure 8: Comparison of experimental data with the model simulations, (a) terminal voltage, (b) current of cell 1 and (c) current of cell 2.

tester, it was not feasible to perform validation over a wide range of SOCs. Controlled SOC decrements, as achieved in HPPC tests, require precise current profiles designed through specialized cell testers. In this simpler setup, such control was not achievable for two parallel connected cells. Nonetheless, the experiment served its primary purpose of generating data to highlight the uneven current distribution in parallel-connected cells and to validate the model and estimation method under realistic operating conditions.

Fig. 9 illustrates the heterogeneities that can emerge in parallel connected battery packs, even when the individual cells are fresh and of the same chemistry (in this case, NMC). During the discharge, the difference between the currents was 21.45%, illustrating the variation between the cells. The net effect of this uneven distribution in currents was that the difference in SOC between the two cells grew by 0.4% over the 440s discharge at 0.3C, despite starting from the same initial conditions. This difference would be even greater if the cells had been initialized with different SOCs. These results demonstrate the need for cell-level estimation if accurate knowledge about the pack is sought.

B. *State-Estimator Performance*

The HP-EKF was then implemented on the experimental setup as shown in Fig. 7 to enable cell level estimation of parallel connected Li-ion battery pack. To ensure the robustness of the proposed approach under realistic conditions, Gaussian noise was added to the dynamic states and measurements. Since there is a dependence between dynamic and algebraic states, the impact of this noise naturally propagates to the algebraic states. The process noise covariance was set to $\mathcal{Q} = 10^{-8}\mathbb{I}_6$, as its magnitude is generally chosen to reflect the expected uncertainty in the system dynamics and is standard in this context, see, for example, [37, see Table II], where the authors have used different sets of process noise covariance. The measurement noise covariance was deliberately chosen to be $\mathcal{R} = 10^{-4}\mathbb{I}_2$ to account for significant measurement uncertainty and evaluate the estimator's performance under such conditions. These choices ensure that the state estimator captures both the inherent dynamics of the system and the uncertainties present in practical implementations. Moreover, the initial error covariance matrix was set to $P_{d,0|0} = 0.0025\mathbb{I}_6$. The system states were initialized at $X_{d,0} = [0.81\ 0\ 0\ 0.80\ 0\ 0]^T$, while the filter was initialized at $\hat{X}_{d,0|0} = [0.815\ 0\ 0\ 0.805\ 0\ 0]^T$. The sampling time T_s was $1s$.

Figs. 10 and 11 present the measured and estimated values of the SOC and local currents for both cells 1 and 2. The estimates obtained from the HP-EKF, a conventional EKF, and a CKF are compared. To ensure a comprehensive evaluation of the proposed HP-EKF, we have conducted Monte Carlo (MC) simulations with 1000 runs, and the resulting RMSEs for SOC and local currents are depicted in Figs. 12 and 13. The results clearly demonstrate a decreasing trend in RMSE over time. Moreover, the numerical values for the average RMSEs of SOC and local currents for both cells are summarized in Table IV. We calculate the average RMSE by first calculating the RMSE and then taking its average over time. The RMSE is calculated as follows:

$$\mathrm{RMSE}_k = \sqrt{\frac{1}{M}\sum_{j=1}^{M}\left(x_{j,k} - \hat{x}_{j,k}\right)^2}, \tag{33}$$

where M is the number of Monte Carlo runs.

These results confirm that the HP-EKF outperforms the conventional EKF in estimation accuracy and performs comparably to the CKF. Additionally, the HP-EKF offers significant advantages over the CKF, particularly in terms of numerical stability [22]. These improvements are particularly important because accurate SOC estimation is critical for optimizing battery usage, preventing overcharging, and extending the battery's lifespan. In practical implementation, these improvements mean that the HP-EKF could improve how the state-estimator deals with the nonlinearities and uncertainties for battery packs in the field, leading to more robust performance in dynamic operating conditions.

The performance of the proposed HP-EKF has been further validated using an additional discharge current profile shown in Fig. 14 to assess its effectiveness under varying conditions. The corresponding results are presented in Figs. 15 and 16. Fig. 15 illustrates the true and estimated SOC values for Cell 1 and Cell 2, while Fig. 16 depicts the true and estimated local currents for the same cells. These results demonstrate the reliability of the HP-EKF in accurately estimating the states across varying discharge conditions.

Moreover, to evaluate the filter's performance under more realistic and dynamic conditions, the HP-EKF was validated using a scaled ARTEMIS urban drive cycle, as shown in Fig. 17 [38], [39]. This profile is characterized by frequent current fluctuations, higher amplitude current transitions, and a broad range of operating conditions—features representative of real-world electric vehicle scenarios. Importantly, the drive cycle spans approximately 90% of the SOC range, thereby covering both linear and nonlinear operating regions. In this case, we

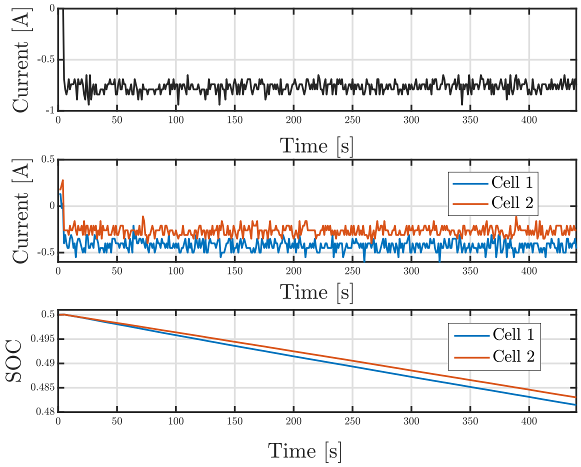

Figure 9: Experimental data of total and individual cell currents as well as SOCs.

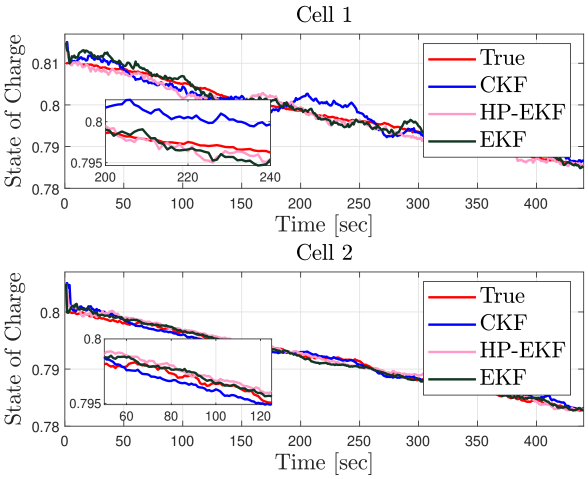

Figure 10: Estimation of SOC in cells 1 and 2.

compared the performance of HP-EKF with both the standard EKF and the CKF, as shown in Fig. 18. As evident from Fig. 18, the results demonstrate that HP-EKF not only outperforms EKF in terms of estimation accuracy but also performs on par with CKF while maintaining lower computational complexity. These findings highlight the robustness and applicability of the HP-EKF for real-time, high-fidelity battery management systems, even under high C-rate and dynamically varying conditions.

Table IV: Average RMSE of SOC and current

Filters	Cell 1		Cell 2	
	SOC	Current (A)	SOC	Current (A)
EKF	0.072	0.105	0.028	0.105
HP-EKF	0.067	0.066	0.023	0.066
CKF	0.068	0.064	0.025	0.064

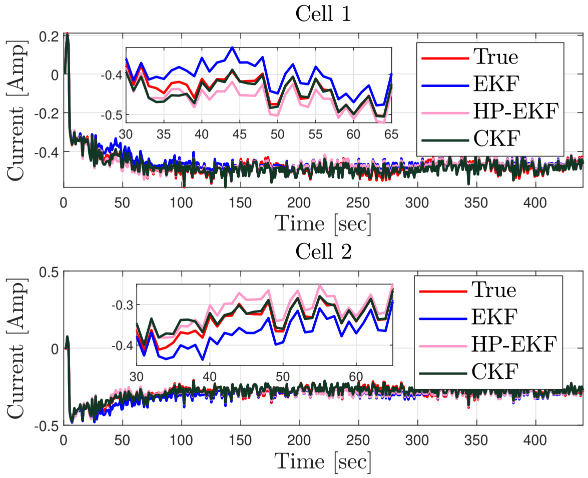

Figure 11: Estimation of current in cells 1 and 2.

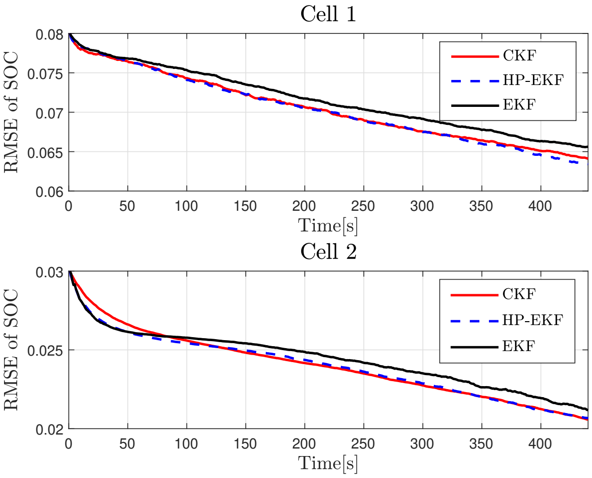

Figure 12: RMSE of SOCs for cells 1 and 2.

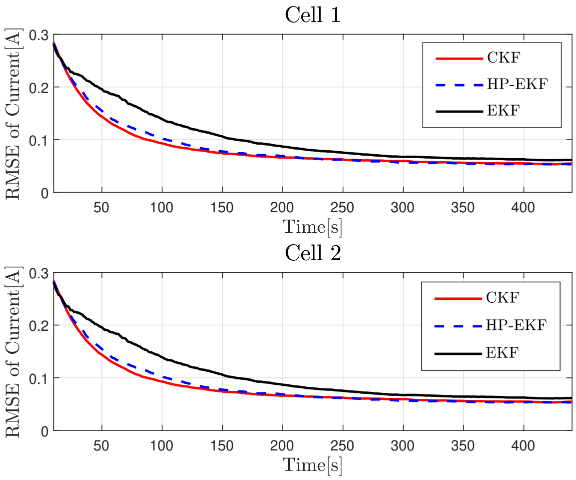

Figure 13: RMSE of currents for cells 1 and 2.

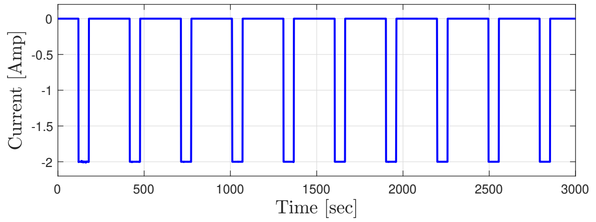

Figure 14: Pulse discharge current profile.

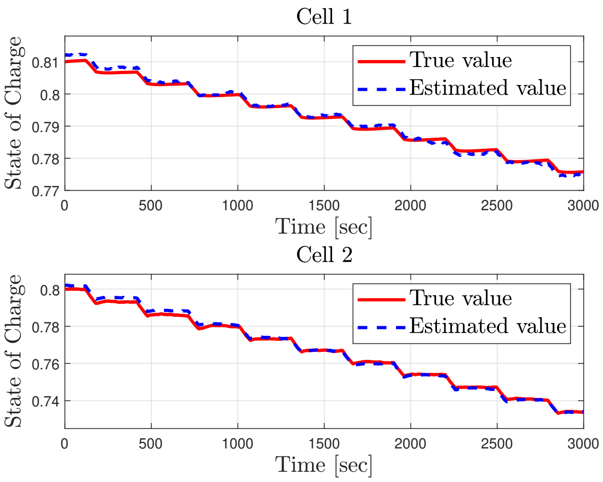

Figure 15: Estimation of SOC in cells 1 and 2.

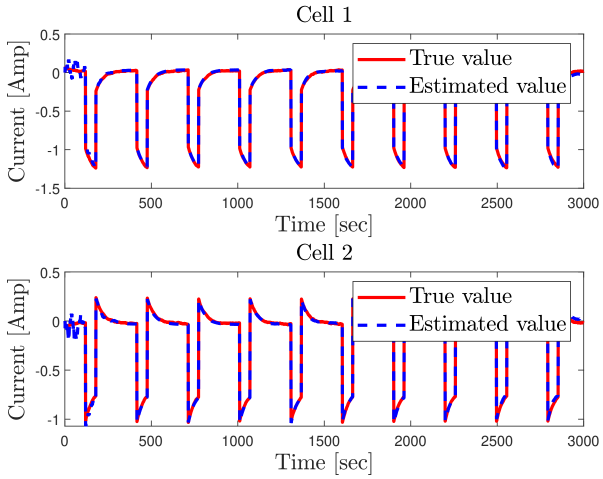

Figure 16: Estimation of current in cells 1 and 2.

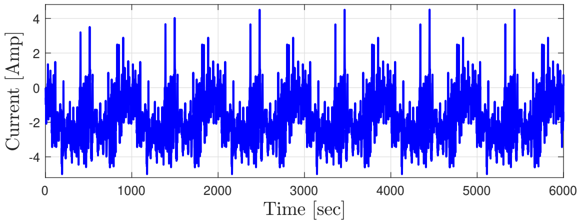

Figure 17: Scaled ARTEMIS urban drive cycle.

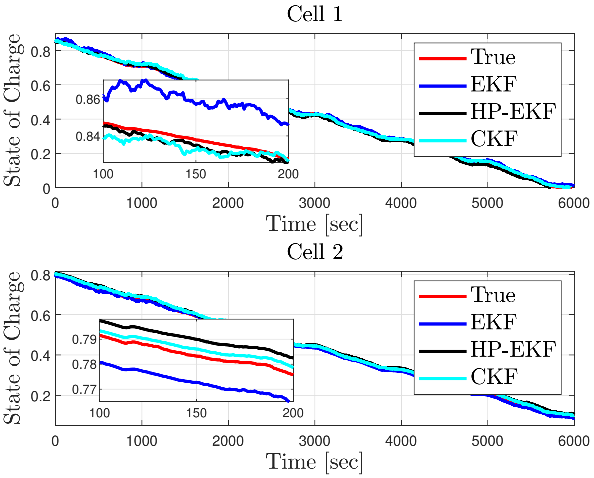

Figure 18: Estimation of SOC in cells 1 and 2 with ARTEMIS urban drive cycle as input.

VII. CONCLUSION

In this paper, a state-estimator for parallel connected lithium-ion battery packs described as a discrete-time non-linear descriptor system was developed. The proposed estimator was an adaption of the EKF and designed for the descriptor system dynamics of the pack whilst also using Hermite polynomials for linearisation to overcome the challenges of propagating the noise forward in time through the nonlinear system. The potential of the proposed estimator was validated on experimental data for NMC-based lithium-ion batteries connected in parallel. The proposed HP-EKF significantly reduced the estimation error compared to the conventional EKF while delivering accuracy comparable to that of the CKF with enhanced numerical stability. The improved estimation performance of the filter underscores its potential for deployment in real-world scenarios to enable smart battery packs to provide information to the BMS about every cell in the pack using only a few sensors. As part of future work, we aim to incorporate thermal dynamics to account for the impact of temperature variations on the performance of the parallel connected battery packs.

REFERENCES

[1] R.E. Ciez and J.F. Whitacre, “The cost of lithium is unlikely to upend the price of Li-ion storage systems,” *Journal of Power Sources*, vol. 320, pp. 310–313, Apr. 2016.

[2] J. T. Frith, M. J. Lacey, and U. Ulissi, “A non-academic perspective on the future of lithium-based batteries,” *Nature Communications*, vol. 14, no. 1, Jan. 2023. Art. No. 420.

[3] M. J. Brand, M. H. Hofmann, M. Steinhardt, S. F. Schuster, and A. Jossen, “Current distribution within parallel-connected battery cells,” *Journal of Power Sources*, vol. 334, pp. 202–212, Dec. 2016.

[4] A.Fill, S. Koch, and K. P. Birke, “Algorithm for the detection of a single cell contact loss within parallel connected cells based on continuous resistance ratio estimation,” *Journal of Energy Storage*, vol. 27, Jan. 2020. Art. No. 101049.

[5] J. P. Ross, E. Chatzinikolaou, D. F. Frost, S. R. Duncan, and D. A. Howey, “Comparison Between Battery Cell Level Dynamics and Pack Level Dynamics Using Equivalent Circuit Models,” in *Proc. of the American Control Conference (ACC)*, July 2024, pp. 713–718.

[6] A. Weng, H. Movahedi, C. Wong, J. B. Siegel, and A. Stefanopoulou, “Current imbalance in dissimilar parallel-connected batteries and the fate of degradation convergence,” *Journal of Dynamic Systems, Mea-*

surement, and Control, vol. 146, Jan. 2024. Art. No. 11106.

[7] C Wong, A Weng, S Pannala, J Choi, JB Siegel, A Stefanopoulou, "Differential Voltage Analysis and Patterns in Parallel-Connected Pairs of Imbalanced Cells," 2024, *arXiv preprint arXiv:2405.17754*.

[8] L. D. Couto, J. Reniers, D. Zhang, D. A. Howey, and M. Kinnaert, "Degradation Monitoring and Characterization in Lithium-Ion Batteries via the Asymptotic Local Approach," *IEEE Transactions on Control Systems Technology*, vol. 33, no. 1, pp. 189–206, Jan. 2025.

[9] T. Bruen and J. Marco, "Modelling and experimental evaluation of parallel connected lithium-ion cells for an electric vehicle battery system," *Journal of Power Sources*, vol. 310, pp. 91–101, Apr. 2016.

[10] S. Sepasi, L. R. Roose, and M. M. Matsuura, "Extended Kalman filter with a fuzzy method for accurate battery pack state of charge estimation," *Energies*, vol. 8, no. 6, pp. 5217–5233, June 2015.

[11] S. Castano, L. Gauchia, E. Voncila, and J. Sanz, "Dynamical modeling procedure of a Li-ion battery pack suitable for real-time applications," *Energy Conversion and Management*, vol. 92, pp. 396–405, Mar. 2015.

[12] D. Huang, Z. Chen, C. Zheng, and H. Li, "A model-based state-of-charge estimation method for series-connected lithium-ion battery pack considering fast-varying cell temperature," *Energy*, vol. 185, pp. 847–861, Oct. 2019.

[13] X. Zhang, Y. Wang, D. Yang, and Z. Chen, "An on-line estimation of battery pack parameters and state-of-charge using dual filters based on pack model," *Energy*, vol. 115, pp. 219–229, Nov. 2016.

[14] X. Chen, H. Lei, and R. Xiong, "A bias correction based state-of-charge estimation method for multi-cell battery pack under different working conditions," *IEEE Access*, vol. 6, pp. 78184–78192, Dec. 2018.

[15] M. Naguib, P. Kollmeyer, and A. Emadi, "Lithium-ion battery pack robust state of charge estimation, cell inconsistency, and balancing," *IEEE Access*, vol. 9, pp. 50570–50582, Mar. 2021.

[16] D. Zhang, L. D. Couto, S. Benjamin, W. Zeng, D. F. Coutinho, and S. J. Moura, "State of charge estimation of parallel connected battery cells via descriptor system theory," in *Proc. American Control Conference (ACC)*, Jul. 2020, pp.2207–2212.

[17] D. Zhang, L. D. Couto, R. Drummond, S. Sripad, and V. Viswanathan, "Cell-level state of charge estimation for battery packs under minimal sensing," 2021, *arXiv preprint arXiv:2109.08332*.

[18] R. Drummond, L. D. Couto, and D. Zhang, "Resolving Kirchhoff's laws for parallel Li-ion battery pack state-estimators," *IEEE Transactions on Control Systems Technology*, vol. 30, no. 5, pp. 2220–2227, Dec. 2021.

[19] Z. Huang, L. D. Couto, C. Dangwal, S. Xiao, W. Lv, D. Zhang, and S. J. Moura, "On Electrochemical Model-Based State Estimation for Lithium-Sulfur Batteries," *IEEE Transactions on Control Systems Technology*, vol. 32, no. 3, pp. 849–861, May 2023.

[20] L. D. Couto, S. M. Schons, D. Coutinho, and M. Kinnaert, "A descriptor system approach for the nonlinear state estimation of Li-Ion battery series/parallel arrangements," *IEEE Transactions on Control Systems Technology*, vol. 31, no. 2, pp. 825–840, Nov. 2022.

[21] D. Zhang, L. D. Couto, P. Gill, S. Benjamin, W. Zeng, and S. J. Moura, "Interval observer for SOC estimation in parallel-connected lithium-ion batteries," in *Proc. American Control Conference (ACC)*, Jul. 2020, pp. 1149–1154.

[22] I. Arasaratnam and S. Haykin, "Cubature Kalman filters," *IEEE Transactions on Automatic Control*, vol. 54, no. 6, pp. 1254-1269, May 2009.

[23] K. Kumar, S. Bhaumik, and P. Date, "Extended Kalman filter using orthogonal polynomials," *IEEE Access*, vol. 9, pp. 59675–59691, Apr. 2021.

[24] I. Sarkas, D. Mavridis, M. Papamichail, and G. Papadopoulos, "Volterra analysis using Chebyshev series," *Proc. IEEE International Symposium on Circuits and Systems*, May 2007, pp. 1931–1934.

[25] E. Süli and D. F. Mayers, *An Introduction to Numerical Analysis*, Cambridge, U.K.: Cambridge University Press, 2003.

[26] F. B. Hildebrand, *Introduction to Numerical Analysis*, New York, NY, USA: Dover, 1987.

[27] I. Arasaratnam and S. Haykin, "Square-root quadrature Kalman filtering," *IEEE Transactions on Signal Processing*, vol. 56, no. 6, pp. 2589–2593, May. 2008.

[28] M. Abramowitz and I. A. Stegun (Editors), *Handbook of Mathematical Functions with Formulas, Graphs, and Mathematical Tables*, Washington, DC, USA: U.S. Govt. Print. Office, 1972.

[29] Y. Wu, D. Hu, M. Wu, and X. Hu, "A numerical-integration perspective on Gaussian filters," *IEEE Transactions on Signal Processing*, vol. 54, no. 8, pp. 2910-2921, Jul. 2006.

[30] S. Bhaumik and P. Date, *Nonlinear Estimation: Methods and Applications with Deterministic Sample Points*, London, U.K.: CRC Press, Jul 24, 2019.

[31] S. S. Bhase, M. Bhushan, S. Kadu, and S. Mukhopadhyay, "Modified extended Kalman filtering for nonlinear stochastic differential algebraic systems," *IFAC-PapersOnLine*, vol. 53, no. 2, pp. 2341–2346, 2020.

[32] S. Bhase, M. Bhushan, S. Kadu, and S. Mukhopadhyay, "Continuous–discrete filtering techniques for estimating states of nonlinear differential-algebraic equations (DAEs) systems," *International Journal of Dynamics and Control*, vol. 11, no. 1, pp. 162–182, Aug. 2022.

[33] Y. Bar-Shalom, X. R. Li, and T. Kirubarajan, *Estimation with Applications to Tracking and Navigation: Theory, Algorithms, and Software*, New York, NY, USA: Wiley, 2004.

[34] R. Karlsson, T. Schon, and F. Gustafsson, "Complexity analysis of the marginalized particle filter," *IEEE Transactions on Signal Processing*, vol. 53, no. 11, pp. 4408–4411, Nov. 2005.

[35] B. Chen, X. Liu, H. Zhao andJ.C. Principe, "Maximum correntropy Kalman filter," *Automatica*, vol. 76, pp. 70–77, Feb. 2017.

[36] W. Li, L. Liang, W. Liu, and X. Wu, "State of charge estimation of lithium-ion batteries using a discrete-time nonlinear observer," *IEEE Transactions on Industrial Electronics*, vol. 64, no. 11, pp. 8557-8565, May. 2017.

[37] M. Proctor, N. Tian, and H. Fang, "State-of-charge estimation for batteries based on the nonlinear double-capacitor model and extended Kalman filter" *in Procs. of IEEE Green Technologies Conference (GreenTech),* Dec. 2020, pp. 10–15.

[38] M. Andre, "The ARTEMIS European driving cycles for measuring car pollutant emissions" *Science of the Total Environment,* vol. 334, pp. 73–84, Dec. 2004

[39] H. Beelen, H. J. Bergveld, and M. Donkers, "Joint estimation of battery parameters and state of charge using an extended Kalman filter: A single-parameter tuning approach," *IEEE Transactions on Control Systems Technology*, vol. 29, no. 3, pp. 1087–1101, May. 2021.